Computational and experimental modulation of a noisy chaotic neuronal system

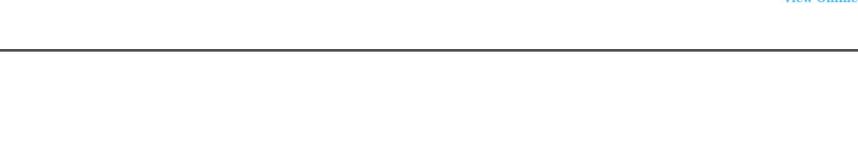
Cite as: Chaos **33**, 033109 (2023); https://doi.org/10.1063/5.0130874 Submitted: 15 October 2022 • Accepted: 13 February 2023 • Published Online: 06 March 2023

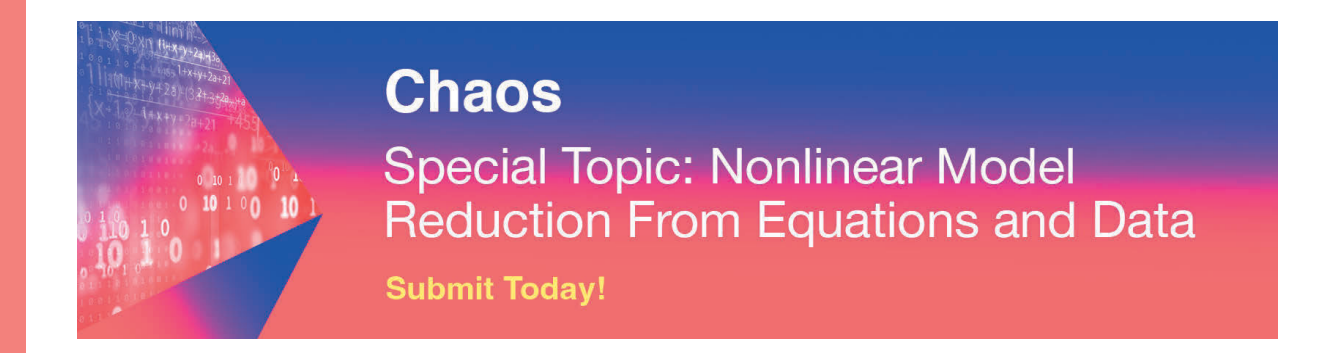














Computational and experimental modulation of a noisy chaotic neuronal system

Cite as: Chaos 33, 033109 (2023); doi: 10.1063/5.0130874 Submitted: 15 October 2022 · Accepted: 13 February 2023 · Published Online: 6 March 2023







Josselyn Gonzalez, 1 📵 Rosangela Follmann, 2, a 10 Epaminondas Rosa, Jr., 1, 3 📵 and Wolfgang Stein 1



- ¹School of Biological Sciences, Illinois State University, Normal, Illinois 61790, USA
- School of Information Technology, Illinois State University, Normal, Illinois 61790, USA
- Department of Physics, Illinois State University, Normal, Illinois 61790, USA

ABSTRACT

In this work, we study the interplay between chaos and noise in neuronal state transitions involving period doubling cascades. Our approach involves the implementation of a neuronal mathematical model under the action of neuromodulatory input, with and without noise, as well as equivalent experimental work on a biological neuron in the stomatogastric ganglion of the crab Cancer borealis. Our simulations show typical transitions between tonic and bursting regimes that are mediated by chaos and period doubling cascades. While this transition is less evident when intrinsic noise is present in the model, the noisy computational output displays features akin to our experimental results. The differences and similarities observed in the computational and experimental approaches are discussed.

Published under an exclusive license by AIP Publishing. https://doi.org/10.1063/5.0130874

Chaotic and stochastic processes, both yielding similar erratic behaviors are, in essence, the result of fundamentally different dynamics: chaotic systems are deterministic and stochastic systems are probabilistic. Despite their absolutely distinct roots, separating intermingled chaotic from stochastic processes poses a rather difficult challenge. In this work, we analyze the behavior of a modulated neuronal nonlinear dynamical system responsible for the gastric function of crustaceans where chaos and stochasticity are intrinsically blended, producing outputs where mixed deterministic and probabilistic dynamics happen to be basically indistinguishable. We focus on the neuronal system responsible for the gastric function in crustaceans, with particular attention on the pyloric dilator neuron of the stomatogastric ganglion of the crab Cancer borealis under the action of neuromodulation. Our approach uses both a computational model without and with noise, and a biological experimental setting. The results we obtain show striking similarities between some of the outputs from the computational and from the experimental studies, despite the inherent difficulty of separating chaos from noise.

I. INTRODUCTION

Chaos is known to be widely present in nature as well as in man-made devices. From Poincaré's landmark work on

the three-body problem in the context of planetary motion, to the unpredictability of the weather² to the complexity of living organisms³ and more, chaos is everywhere.⁴⁻⁶ In the case of neuronal systems, chaotic behavior has been observed in a multitude of situations,^{7,8} particularly when neurological processes undergo transitions between states of tonic and bursting regimes. Neuronal transitions have been investigated in computational studies⁹⁻¹² as well as in experimental settings where transitions have been found in thalamocortical neurons during sleep cycles, 13 in Parkinson's disease tremors typically generated in sensory-motor nuclei,14 in silent or tonic to bursting transitions in motor neurons when animals start to move as well as during gait-speed changes, 15-17 and also in central pattern generators (CPGs) controlling the stomatogastric system in crustaceans where robust and continuous activity is of essence for the survival of the animal. ^{18,19} In this system, various motor patterns have been described that are under modulatory control by hormones and neuromodulatory transmitters via paracrine release. 19-22 Individual neurons of the stomatogastric ganglion (STG) transition between silent, tonic, and various rhythmic activities that are heavily dependent on the modulatory substances that reach the STG. The individual neuronal activity modes and their respective brain states have been studied extensively. Most of these different activity modes exist along a continuum, and it appears that while present, chaos is suppressed by strong synaptic circuit feedback in stomatogastric neurons.²³ Much less is known about the transitions between

a)Author to whom correspondence should be addressed: rfollma@ilstu.edu

activity states, and it is unclear which dynamics drive them. Transitions are typically characterized by seemingly erratic firing activity that is distinct from the activities before and after the transition. Computational models have demonstrated that many transitions are mediated by chaos, ^{10,12,24,25} while experimental evidence from biological neuronal systems is rare and often hampered by the presence of noise. Here, we use computational and experimental approaches to characterize different activities displayed by neurons when subjected to neuromodulation, and the transitions between these activities. The combination of the computational and experimental methods employed in this work allows us to perform a direct comparison between the model and biological system and characterize the dynamics displayed by both.

Computationally, we employ a Hodgkin-Huxley-type neuronal model with an added modulation-induced current, the equivalent of a current that is known to produce rhythmic activity in STG neurons.²⁶ We find transitions between silent, bursting, and tonic regimes that happen through period-doubling bifurcation cascades into chaos. These transitions, however, are less evident when intrinsic noise is introduced in the model equations, with the period-doubling bifurcation cascade no longer visible. The noisy computational output, however, displays striking similarities with experimental data obtained from the crustacean CPG neuron, suggesting that chaos potentially present in the experimental setting may be hidden in the midst of noise. Our computational model displays results consistent with intracellular recordings obtained from experiments in which the modulatory current was injected into STG CPG neurons using dynamic clamp in the synaptically isolated pyloric dilator (PD) neuron of the stomatogastric nervous system of the crab Cancer borealis.

This manuscript is organized as follows. In Sec. II, we introduce the Huber–Braun model equations for the single neuron and in Sec. III we introduce the modulatory induced current term that is known to affect the rhythmic activity of CPG neurons. In Sec. IV, we add intrinsic noise to the neuron model and in Sec. V, we show an experimental neuronal transition induced by a neuromodulatory input, along with the experimental and computational Poincaré maps in Sec. VI. Final comments are presented in Sec. VII.

II. NEURONAL MODEL EQUATIONS

The mathematical model used in this study is based on the Hodgkin–Huxley equations and was first introduced to study temperature-sensitive neurons. The so-called Huber–Braun model consists of four ordinary differential equations with time-dependent state variables describing the cell's membrane potential V, potassium fast activation $a_{\rm K}$, and two slow activation variables, $a_{\rm SR}$ for potassium and $a_{\rm SD}$ for sodium,

$$C\dot{V} = -I_{L} - I_{Na} - I_{K} - I_{SD} - I_{SR} - I_{inj},$$
 (1)

$$\dot{a}_{\rm K} = \frac{\phi}{\tau_{\rm K}} \left(a_{\rm K\infty} - a_{\rm K} \right), \tag{2}$$

$$\dot{a}_{\rm SR} = -\frac{\phi}{\tau_{\rm SR}} \left(\nu_{\rm acc} I_{\rm SD} + \nu_{\rm dep} a_{\rm SR} \right),\tag{3}$$

$$\dot{a}_{\rm SD} = \frac{\phi}{\tau_{\rm SD}} \left(a_{\rm SD\infty} - a_{\rm SD} \right). \tag{4}$$

In these equations, C and I_{inj} represent, respectively, the membrane capacitance and injected current stimulus. Leak channels have been demonstrated to be voltage-dependent, but for the purpose of this work we approximate the leak current as ohmic, writing it as $I_L = g_L(V - V_L)$ where g_L is the leak conductance, and V_L is the corresponding equilibrium potential. The fast and slow currents for sodium and potassium mentioned above and labeled Na, K, SD, and SR, respectively, are written as $I_i = \rho g_i a_i (V - V_i)$, where j denotes Na^+ , K^+ , SD, or SR. V_i represents the equilibrium potential for each corresponding current, and the temperature dependent scaling parameters are fixed (check the Appendix for parameter values). The maximum conductances and half-activation potentials are represented by g_i and V_{0i} , respectively. Characteristic time constants τ_i control the opening and closing of the various ion channels, with the sodium channels in particular considered to be activated rather quickly, with an activation function given by $a_{\rm Na} =$ where s_{Na} sets the slope of the sigmoidal curve, and $V_{0_{\text{Na}}}$ corresponds to the half-activation potential. The activation func-

responds to the half-activation potential. The activation functions $a_{j\infty}$ are mimicked by sigmoidal steady state curves given by $a_{j\infty} = \frac{1}{1+e^{-5}(V-V_0_j)}$, j = K, SD, SR. In this model $a_{Na} \equiv a_{Na\infty}$, as a result of the very fast Na⁺ channel activation, and Ca⁺⁺ accumulation and depletion are, respectively, included in ν_{acc} and ν_{dep} . Inactivation is included in the functional timing of the activation functions of the corresponding conductances.

This is the Huber-Braun neuronal model and has been applied to investigate a variety of topics, including temperature effects in neuronal dynamics, 11,28 synaptic transmission in psychiatric disorders,²⁹ reciprocal inhibition and electrical coupling in CPG neurons,9 and tonic-bursting transitions (in networked neurons) mediated by gap junction strength. 10,12 The Huber-Braun single neuron model is able to mimic a wide range of neuronal behaviors including tonic, bursting, and chaotic spiking modes. Figure 1(a) shows these rich changes in dynamics for a range of the slow repolarizing conductance g_{SR} and the slow depolarizing conductance g_{SD} , with no injected current ($I_{inj} = 0 \,\mu\text{A/cm}^2$). The different colors represent regions with membrane potentials displaying dynamic behaviors of tonic (teal), chaotic bursting (red), periodic bursting (yellow, green, blue, black), subthreshold oscillations (purple) and silent resting potential (gray). The model neuron's average firing rate for the same parameter space of Fig. 1(a) is illustrated in the color map of Fig. 1(b), showing generally that for a fixed g_{SD} with increasing g_{SR} , the neuron's firing rate goes down. Conversely, for a fixed g_{SR} with increasing g_{SD} , the neuron's firing rate goes up. For a sample close-in view, we select a cross section in Fig. 1(a) at $g_{SD} = 0.2 \text{ mS/cm}^2 \text{ with } 0.1 \text{ mS/cm}^2 \le g_{SR} \le 0.3 \text{ mS/cm}^2$ [dashed white line in Fig. 1(a)], which shows the neuron's dynamics starting tonic, traversing regions of various firing patterns and subthreshold oscillations, and ending with the resting potential. The corresponding bifurcation diagram is displayed in Fig. 1(c) with the interspike intervals on the left-hand side scale and graph in black, and the firing rate on right-hand side scale with the line shown

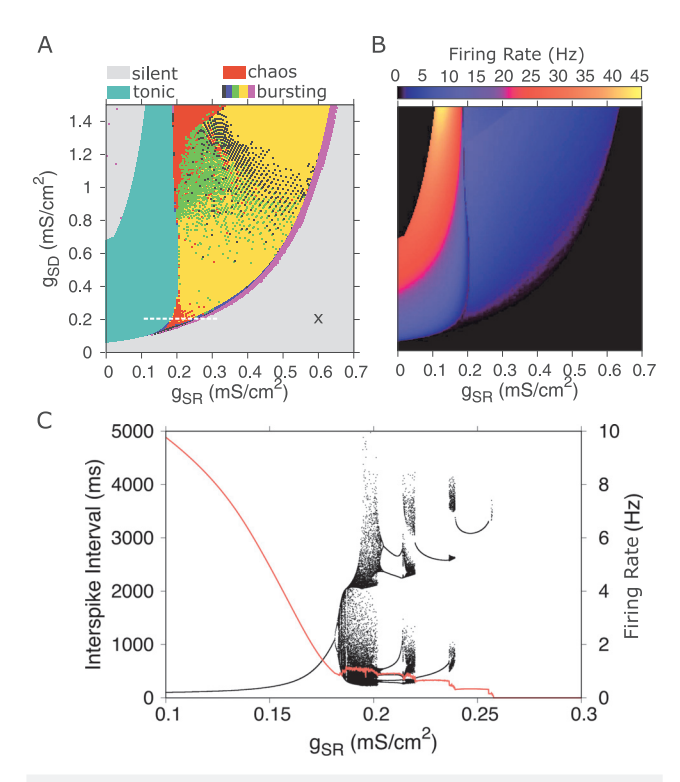


FIG. 1. Color maps for the pattern outputs (a) and firing rate (b) of the Huber–Braun neuron model with a range of values of the conductances g_{SR} and g_{SD} . (c) Bifurcation diagram for increasing values of g_{SR} and $g_{SD} = 0.2\,\mathrm{mS/cm^2}$. The injected current $I_{inj} = 0\,\mu\mathrm{S/cm^2}$. The marker "x" in plot (a) indicates the g_{SR} and g_{SD} values used to represent the neuron in Figs. 2 and 3. The pattern outputs of the model are silent (gray), tonic (teal), chaoc (red), and bursting (yellow, light green, blue, black, pink) following the color scheme presented in Ref. 9. Yellow: periodic bursting, light green: periodic bursting with alternating one and two spikes per subthreshold oscillation, blue: one spike per subthreshold oscillation, black: one spike every other subthreshold oscillation, pink: subthreshold oscillation with no spikes. This same color scheme is used in Figs. 2(a) and 3 pattern color maps.

In what follows, the characteristics encountered in the graphs of Fig. 1 will be further explored with the model equations displaying an additional current I_{MI} for induced modulation.

III. MODULATORY INDUCED CURRENT

The crustacean STG controls different aspects of feeding behavior, and its neurons exhibit distinct activity modes under diverse modulatory conditions. 30,31 Proctolin, for example, is a well-characterized neuropeptide that restores a stable rhythmic activity in decentralized or weakly active STG neurons. 32 Proctolin produces state-dependent actions via a depolarizing, nonspecific cation current called modulator-induced current, or I_{MI} , that facilitates oscillations in the membrane potential of bursting neurons. 33,34 To investigate the effects of I_{MI} in the model, we include I_{MI} in Eq. (1),

$$C\dot{V} = -I_{\rm L} - I_{\rm Na} - I_{\rm K} - I_{\rm SD} - I_{\rm SR} + I_{\rm inj} - I_{\rm MI},$$
 (5)

expressed as $I_{MI} = g_{MI}a_{MI}(V-V_{MI})$, where g_{MI} is the maximal conductance of the current, with the reversal potential set to $V_{MI} = 0 \, \mathrm{mV}$. The modulatory activation function is given by $a_{MI} = \frac{1}{1 + \exp\left(\frac{V-V_{0MI}}{V}\right)}$, where $V_{0MI} = -40 \, \mathrm{mV}$ and $s = -10 \, \mathrm{mV}$.

To obtain a better understanding of the effects of I_{MI} using our model, we first look at the combined actions of the modulatory-induced current I_{MI} and the neuronal model's excitability I_{inj} for enabling neuronal transitions. Excitability is an intrinsic feature of neurons, allowing them to generate action potentials which is crucial for signal propagation and proper functioning of neuronal circuits. The Levels of excitability of a cell also determine the state-dependent effects of proctolin. That is, proctolin's effects diminish with higher baseline neuronal excitability. The state-dependent effects of proctolin excitability.

Figure 2 shows the outcomes of varying g_{MI} at different values of I_{inj} . Each point in Fig. 2(a) corresponds to the state resulting from a particular pair of values for g_{MI} and I_{inj} , with the whole color map summarizing the activity states of the model

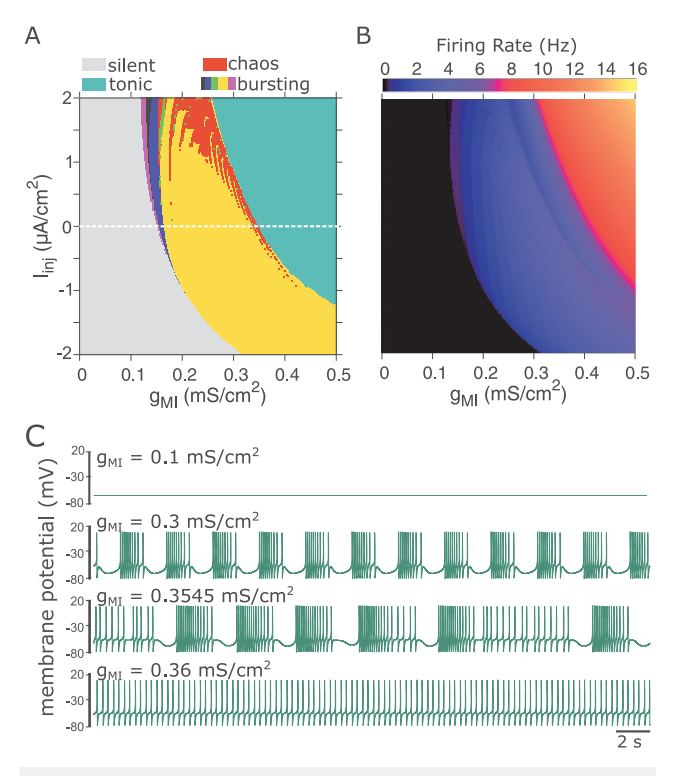


FIG. 2. (a) Firing pattern color map showing the computational model results with varying g_{Ml} and the injected current I_{inj} . I_{Ml} -induced transitions and the amount of chaos in these transitions depend on the excitability level of the cell. Yellow indicates bursting activities, teal indicates tonic, and red indicates chaos. The dashed line at $I_{inj} = 0~\mu$ S/cm² indicates the cross section used for the bifurcation diagram shown in **Fig. 4**. (b) Corresponding frequency color map for the different firing patterns displaying in (a). The baseline neuron dynamics is silent with $g_{SR} = 0.6~\text{mS/cm}^2$ and $g_{SD} = 0.2~\text{mS/cm}^2$. (c) Neuronal model voltage traces for different g_{Ml} values. With $g_{Ml} = 0.1$, 0.3, 0.3545, and 0.36 mS/cm², the model produces silent, bursting, chaotic, and tonic activities, respectively.

neuron over the specified range of parameter values. Following the same color convention of Fig. 1(a), yellow, green, and blue, for example, indicate bursting activities, while teal indicates tonic activity. Red indicates chaotic regimes, which are typically located between the bursting and tonic regions in Fig. 2(a) [see also Fig. 1(a)], where the tonic-bursting transition takes place. Lower firing rates characterize this region, noticeable in Fig. 2(b) by the darker curved valley area in the violet region starting at $I_{inj} = 2 \text{ mS/cm}^2$ and $g_{MI} = 2.5 \text{ mS/cm}^2$, bending to the right as I_{inj} decreases and g_{MI} increases. In this transition, the firing rate trend downward reverses temporarily to upward. 12 More excited neurons ($I_{inj} > 0 \,\mu\text{S/cm}^2$) reach the bursting-tonic transition at lower g_{MI} values than neurons with lower excitation $(I_{inj} < 0 \,\mu\text{S/cm}^2)$. Concurrently, the bursting regime diminished with more excitation. Figure 2(a) also shows that the range of g_{MI} for busting (yellow) decreased and the range of g_{MI} for tonic activity (teal) increased with more excitation. More excited neurons went through larger regions of chaos during the bursting-to-tonic transition than less excited ones, as indicated by larger areas of red on the upper part of Fig. 2(a). Overall, these results show that, consistently with the known state-dependence of proctolin modulation in the STG, 32 the effect that g_{MI} has on the model neuron activity depends on the excitability state of that neuron.

The map of spiking rate [Fig. 2(b)] shows lower frequencies throughout the bursting region (shades of purple) increasing in chunks (more noticeably along the g_{MI} axis for a fixed $I_{inj} = 0.5 \,\mu\text{A/cm}^2$, for example), while the tonic region shows that frequencies increases smoothly and faster for increasing g_{MI} (red-orange-yellow). For higher levels of excitability $(I_{inj} > 0 \,\mu\text{S/cm}^2)$, the magnitude of g_{MI} that is needed to induce a transition from bursting to tonic is less than what is needed for lower levels of excitability (I_{inj} < 0 μ S/cm²). Also, more excited neurons went through larger regions of chaos during this transition than less excited ones (red areas). Overall, these results show that the effect that g_{MI} has on the neuron model activity depends on the state of the neuron, with higher cell excitability facilitating the occurrence of chaos. Four samples of voltage outputs with different dynamics are displayed at the bottom of Fig. 2, for the respective g_{MI} values, all in units of mS/cm²: 0.1 (silent, graph C), 0.3 (bursting, graph D), 0.3545 (chaos, graph E), and 0.36 (tonic, graph F).

In addition to the injected current, the interplay between g_{SR} and g_{SD} also determines the neuron's activity state, as they represent the wide range of ionic conductance levels that biological neurons may exhibit.³⁶ To assess the combined effects of changing these conductances on I_{MI} -induced transitions, we analyzed the parameter space varying g_{MI} , I_{inj} , g_{SR} , and g_{SD} independently (Fig. 3). In this figure, each individual color map shows the neuronal activity patterns for different combinations of g_{SR} and g_{SD} values. Horizontally across, the five color maps differ by values of I_{ini} (values indicated on the top of the color maps). Vertically across, they differ by values of g_{MI} (values indicated on the right-hand side of the color maps). The white crosshairs on each map indicate $g_{SR} = 0.6 \,\mathrm{mS/cm^2}$ and $g_{SD} = 0.2 \,\mathrm{mS/cm^2}$, the values used to create the color maps in Fig. 2 and the bifurcation diagram in Fig. 4. Following the crosshairs across maps, we observed that increasing g_{MI} was sufficient to induce transitions from silent to bursting and tonic activities. This is consistent with the results from Figs. 2 and 4, but also with the ability of I_{MI} to generate bursts in STG neurons.³⁷

We also observe that with more excitation (larger I_{inj}), less g_{SD} was required to elicit bursting and tonic activities, a consequence of I_{inj} and g_{SD} both being excitatory. However, our results also demonstrate that cell excitability facilitated the appearance of chaos. With larger I_{inj} , chaos occurred at almost all borders between the bursting and tonic regimes. This was noticeable from the elongated red area along the transition line between bursting (yellow) and tonic (teal) activity. Two main areas of chaos were visible: one between $g_{SD} = 0.3 \,\mathrm{mS/cm^2}$ and $0.5 \,\mathrm{mS/cm^2}$ and the other between $g_{SD} = 0.8 \,\mathrm{mS/cm^2}$ and $1.6 \,\mathrm{mS/cm^2}$. With less excitation (smaller/ negative I_{inj}), chaos became restricted to high g_{SD} values and was absent below $g_{SD} = 1 \text{ mS/cm}^2$. Nevertheless, the total occurrence of chaos in this parameter range increased, as measured by the area occupied by the red color. Thus, more excitation made chaos more likely to occur at the boundary between the bursting and tonic activity states, albeit in an overall smaller parameter space.

Increasing g_{MI} made bursting more likely, as indicated by the enlarged yellow regions in the color maps of Fig. 3. Simultaneously, the size of the chaotic regions (in red) changed. For example, without injected I_{inj} and modulatory I_{MI} currents, two clearly separated areas of chaos were present, one around $g_{SD} = 0.2 \,\mathrm{mS/cm^2}$ and another between $g_{SD} = 1.0$ and $1.5 \,\mathrm{mS/cm^2}$. Increasing I_{MI} resulted in increased upper and a decreased lower chaotic regions spanning from $g_{SD} = 0.7$ to 1.5 mS/cm², however the chaotic region doubled in size as g_{MI} becomes nonzero. This can be seen by measuring the the relative size of the respective areas with respect to the total area of the map. With 3.92% at $I_{inj} = 0 \mu \text{A/cm}^2$ and $g_{MI} = 0 \text{ mS/cm}^2$; 8.72% at $I_{inj} = 0 \,\mu$ A/cm² and $g_{MI} = 0.4 \,\text{mS/cm}^2$. Overall, the larger regions of chaos are associated with larger g_{MI} and g_{SD} values, and tonicbursting transitions were more likely when increasing g_{MI} . However, decreasing excitation through negative I_{inj} , chaos became restricted to fewer bursting-to-tonic transitions, i.e., those at high g_{SD} levels. Thus, with this restricted region of chaos, there are fewer options within the parameter space that result in a chaotic transition.

To further explore and better understand the underlying mechanisms mediating these transitions, we generated a bifurcation diagram for neuronal interspike intervals and firing rates, using the conductance g_{MI} as the control parameter. The diagram is displayed in Fig. 4(a), allowing the visualization of the neuronal changes in activity patterns (left vertical scale, green graph) along with the corresponding changes in firing rate (right vertical scale, red graph) for a range of g_{MI} values. For low levels of g_{MI} , between 0 and 0.15 mS/cm², the neuron does not spike. At $g_{MI} \approx 0.15$ mS/cm², the neuron begins to burst, initially at a very low firing rate that increases as the spikes per burst increase by one spike at a time, this pattern is more clearly visible in the interspike interval graph. This trend continues up to $g_{MI} \approx 0.3534$ mS/cm² where the firing rate reaches 5 Hz, drops suddenly, and continues to increase in an overall approximately linear fashion.

The bursting-to-tonic transition for $0.353 \text{ mS/cm}^2 \leq g_{MI} \leq 0.360 \text{ mS/cm}^2$ denoted by the dashed rectangle in the bifurcation diagram in Fig. 4(a) is shown zoomed in in Fig. 4(b). In this range, there is a region of chaotic behavior, which includes the typical windows of periodicity and the frequency dropping down sharply from 5 to 3 Hz, followed by an inverted period doubling cascade for

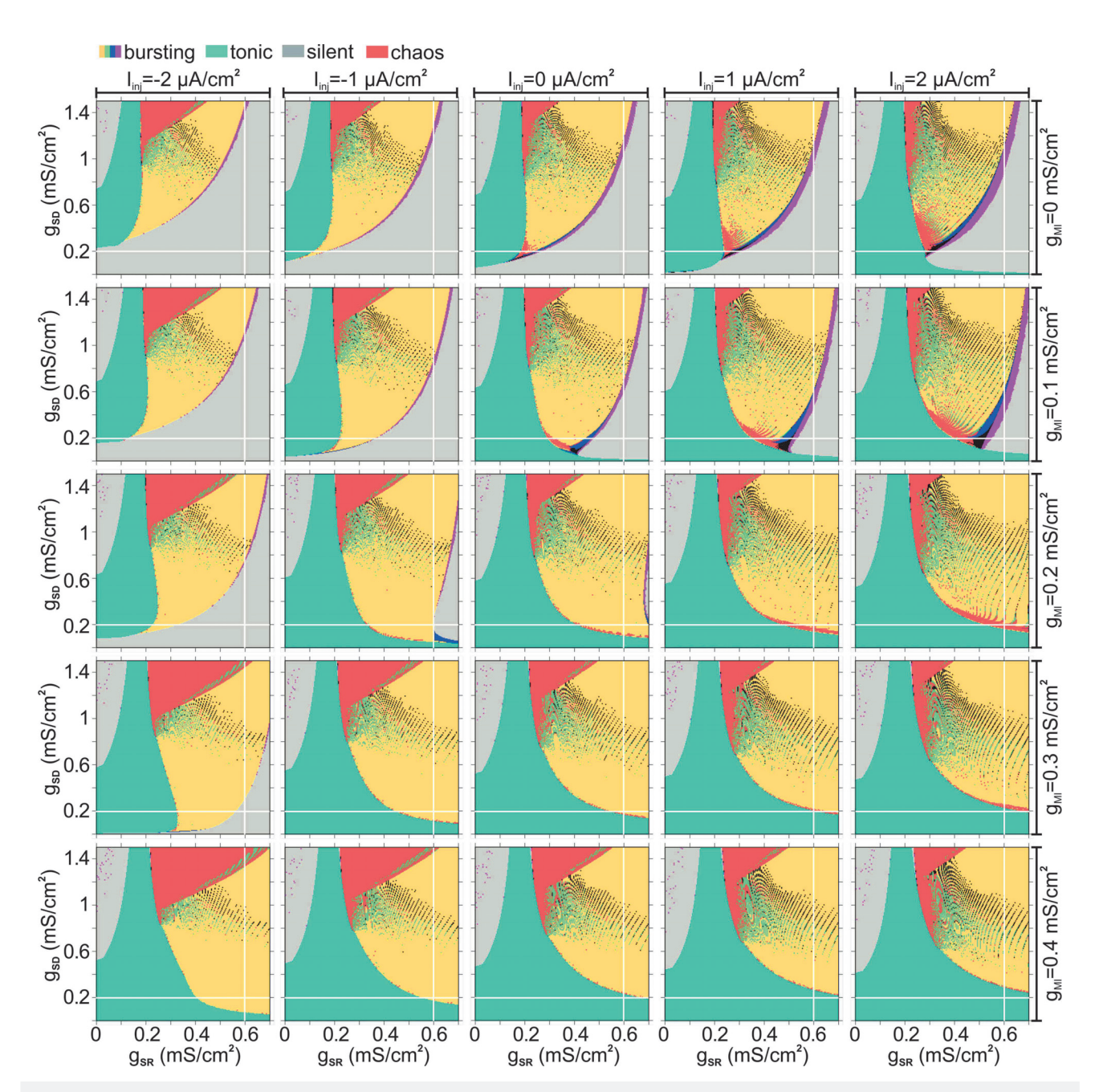


FIG. 3. Color maps showing activity types of models with discrete values of g_{Ml} and l_{inj} , g_{SR} , and g_{SD} . Each color map shows discrete models with varying g_{SD} and g_{SR} values. Horizontally across, there are 5 l_{inj} conditions. Vertically across, there are 5 g_{Ml} conditions. White-cross hairs: $g_{SR}=0.6\,\mathrm{mS/cm^2}$ and $g_{SD}=0.2\,\mathrm{mS/cm^2}$, the values used in Figs. 2 and 4.

 $0.356~{\rm mS/cm^2} \le g_{MI} \le 0.3592~{\rm mS/cm^2}$. A tonic spiking regime follows for g_{MI} larger than $0.3562~{\rm mS/cm^2}$, with the firing rate back into its upward trend, up to $10~{\rm Hz}$ at $g_{MI} = 0.5~{\rm mS/cm^2}$. These results further illustrate the modulation elicited bursting-tonic transition

mediated by chaos. This shows that the tonic-to-bursting transition induces a decrease in the tonic firing rate to its lowest value, followed by a short-lived firing rate increase in the chaotic regime, and afterwards resuming its trend toward lower firing rates in the

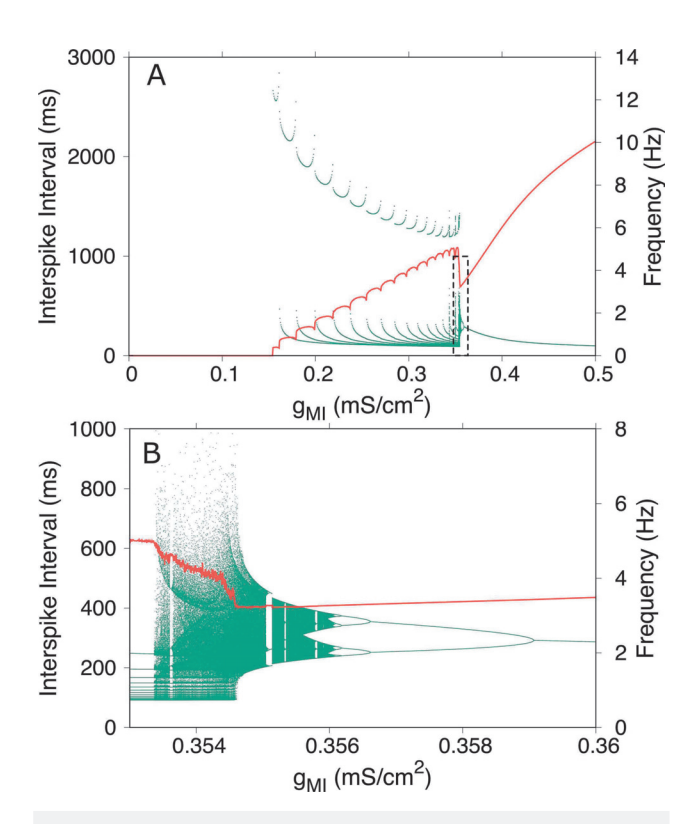


FIG. 4. Bifurcation diagram (green) and firing rate (red) with g_{Ml} as the bifurcation parameter for $I_{inj}=0$. Increasing g_{Ml} , elicited activity transitioning from silent to bursting to tonic. (b) Zooming in of graph in Fig. 3(a) for 0.353 mS/cm² $\leq g_{Ml} \leq 0.36$ mS/cm². The magnification reveals in more details the bursting-to-tonic transition with chaos and an inverted period doubling cascade, indicating a chaos mediated transition.

bursting regime.¹¹ Additionally, the period doubling and period adding (in the bursting regime) features observed here with g_{MI} as the control parameter, have also been previously obtained with g_{SR} ³⁸ and temperature³⁹ as the control parameter.

Taken together, the above model results show that I_{MI} induces transitions between silent, bursting, and tonic activity states. Additionally, the transition between bursting to tonic occurs through a period-doubling cascade and chaos. How I_{MI} induces bursting-to-tonic transitions is dependent on the excitability level and the balance of conductances of the model neuron. Not only do these properties alter how much I_{MI} is needed to induce a transition, they also determine the size and location of the chaotic region within the transition.

IV. NOISE

Biological systems are intrinsically noisy with neuronal systems not being an exception. Stochastic fluctuations in neurons result in part from the cell membrane's peculiar properties, including the opening and closing mechanisms of ion channels.^{40,41} We embedded stochasticity in our modulated neuronal equations by introducing

one more term, $\zeta(t)$, in the currents equation [Eq. (5)] to obtain

$$C\dot{V} = -I_{\text{leak}} - I_{\text{Na}} - I_{\text{K}} - I_{\text{sd}} - I_{\text{sr}} - I_{\text{inj}} - I_{\text{MI}} - \zeta,$$
 (6)

where the Box–Muller algorithm²⁸ was used to numerically implement the Gaussian white noise term

$$\zeta(t) = \left[\frac{-4D}{\Delta t} \ln(a) \right]^{1/2} \cos(2\pi b), \tag{7}$$

where D is the noise intensity, Δt is the time step of integration, with uniformly distributed random numbers a and $b \in [0,1]$, and statistics $\langle \zeta(t) \rangle = 0$ and $\langle \zeta(t) \rangle \langle \zeta(t') \rangle = 2D\delta(t-t')$. The effect of noise on the neuron model bifurcation diagram for three different noise intensity levels is shown in Fig. 5. In each of the three cases, the neuron remains silent for a range of g_{MI} between 0 and ≈ 0.15 mS/cm², at which point the neuron exhibits two distinct bands of interspike intervals. These eventually merge into a single band at different g_{MI} values for each noise level.

The noisy bifurcation diagrams shown in Fig. 5 retain the overall features of the noise-free neuron, except that the typical chaotic transition clearly displayed in Fig. 4 is no longer visible in the bifurcation diagrams of Fig. 5. In particular, the characteristic kink found in the firing rate graph during the tonic-bursting transition 10,42 is not present for large values of the noise intensity D. We also observe that larger values of g_{MI} are needed for the noisy system to transition from bursting to tonic. Nonetheless, there are notable similarities between the noisy and the noise-free systems, in the frequency plots (red) scaled on the right-hand sides of Figs. 4 and 5, both plots exhibit overall increasing firing rates for increasing values of g_{MI} with the drop in frequency present in the noiseless case not visible in the noisy system except for the small D = 0.01 case. However, we can see a change in the slope of the noisy diagram at the point where the chaotic transition would be expected to happen, at $g_{MI} \approx 0.42 \,\mathrm{mS/cm^2}$. From that point on, the slope of the noisy frequency graph increases and then curves back showing a trend toward a less steep upward slope. This behavior is the same observed for the noiseless frequency graph right after the transition in Fig. 4. Additionally, ISI histogram graphs (Fig. 5 insets) illustrate how the various peaks diminishes as the noise is increased. These results suggest that the typical chaos found in the tonic-bursting transition region was absorbed in the stochasticity of the noisy system.

V. EXPERIMENTAL DYNAMIC CLAMP

We test our computational model results described above on a biological experimental setting using dynamic clamp current injected in a synaptically isolated biological neuron of the STG of the crab *C. borealis* [Fig. 6(a)]. The STG controls different aspects of the animal's feeding behavior, and its neurons display distinct activity states under different modulatory conditions. ^{30,31} The ganglion is innervated by descending modulatory projection neurons that originate in the commissural ganglia (CoGs) [Fig. 6(a)]. Release of neuromodulators by these projection neurons contributes to the generation and maintenance of rhythmic activities of the neurons in the STG network. The pyloric circuit produces a tri-phasic rhythm¹⁹ [Fig. 6(b)] that includes the activities of the pyloric dilator (PD), lateral pyloric (LP), and pyloric constrictor (PY) neurons. The PD neurons are part of the pacemaker group that drives the pyloric

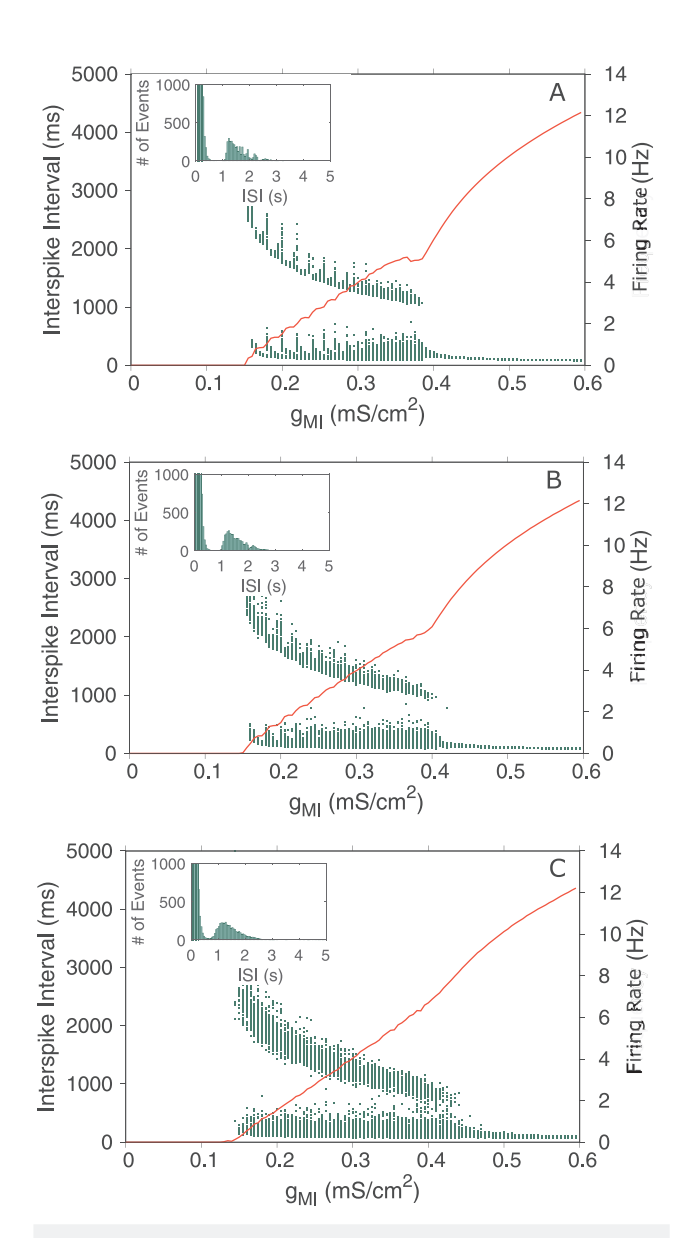


FIG. 5. Computational bifurcation diagrams (green) for the noisy model neuron with g_{Ml} as control parameter with noise amplitude values D=0.01 in (a), D=0.05 in (b), D=0.5 in (c). The red line refers to the corresponding firing rate in the three cases, showing the decline and erasure of the typical downward kink in the transition region for increasing values of the amplitude D. The insets show the corresponding ISI histograms for each of the three graphs.

rhythm and determines the pyloric cycle period. LP and PY are follower neurons with LP providing the sole feedback synapse to the pyloric pacemakers. Removal of modulatory input via pharmacology or transection of projection neuron axons causes the pyloric neurons to become arrhythmic or silent.³¹ Both applying a neuromodulator such as proctolin for example,⁴³ or introducing the ionic

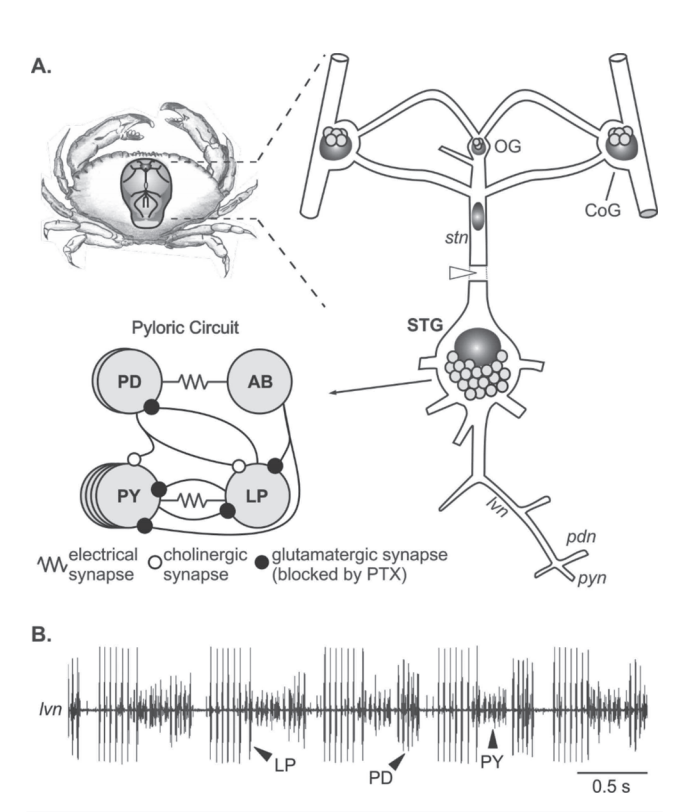


FIG. 6. (a) Schematic of the isolated stomatogastric nervous system (right) of the crab *C. borealis* (left). The STG contains 26 easily identifiable neurons that are innervated through the *stn* (stomatogastric nerve) by descending projection neurons originating in the OG (esophageal ganglion) and CoGs (commissural ganglion). In this experiment the *stn* was transected. The axons of the STG motor neurons project through the posterior nerves, including the *lvn* (lateral ventricular nerve), the *pdn* (pyloric dilator nerve), and the *pyn* (pyloric constrictor nerve); (stomatogastric ganglion). Bottom left: The core circuit driving the pyloric rhythm in the STG containing the AB (anterior burster neuron), the PD (pyloric dilator neuron), the LP (lateral pyloric neuron), and the PY (pyloric constrictor neuron). (b) Extracellular recording of PD, LP, and PY neurons on the *lvn*. Our focus here is on the PD neurons.

conductance elicited by proctolin via dynamic clamp, can restore neuronal activity. Used extensively in electrophysiology, dynamic clamp consists of implementing a real-time interface between the living cell and a computer to simulate dynamical processes.⁴⁴

For the purpose of this work and given its prominent role in the STG circuit, we selected the PD neuron for our experimental study of the tonic-bursting transition. Intracellular recordings performed using a dynamic clamp injected current on the synaptically isolated PD neuron³⁴ yield experimental outputs equivalent to those obtained from the numerical simulations performed with the computational model using the neuromodulatory current I_{MI} . Therefore, after synaptically isolating the PD neuron in our experiment, a dynamic clamp current mimicking I_{MI} was injected into the biological neuron using a two-electrode setup.^{34,45} The mathematical model for the dynamic clamp current I_{MI} is based on the ohmic

current equation

$$I_{MI} = g_{MI} \cdot a_{MI} \cdot (V - V_{MI}), \tag{8}$$

where g_{MI} is the maximum conductance, a_{MI} is the activation function, V_{MI}) is the equilibrium potential, and V is the membrane potential of the cell. The implemented current–voltage relationship is given by

$$I_{MI} = \begin{cases} 0 & \text{for } V < -70, \\ -0.7 \cdot g_{MI} \cdot (V + 70) & \text{for } -70 \le V < -40, \\ -21 \cdot g_{MI} & \text{for } -40 \le V \le -20, \\ g_{MI} \cdot (V - 0) & \text{for } V > -20. \end{cases}$$

The calculations were run in real-time in a Micro-1401 (CED, UK) sequencer with the conductance g_{MI} increased by a fixed amount every 100 s, with voltage traces across the membrane being collected for a range of g_{MI} values. Four samples are depicted in Fig. 7, with $g_{MI} = 0$ nS (silence), $g_{MI} = 54$ nS (bursting), $g_{MI} = 85$ nS (chaotic), and $g_{MI} = 114$ nS (tonic). These voltage traces display clear resemblance with the voltage traces of the computational model [Fig. 2(c)].

The data collected were processed to extract the interspike intervals for each run of the different values of g_{MJ} , from which we

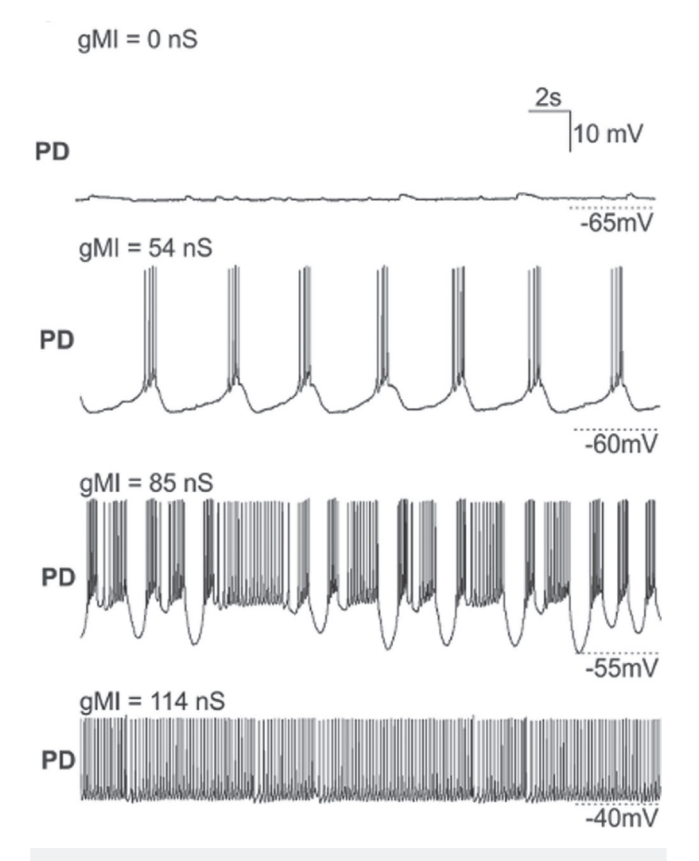


FIG. 7. Experimental voltage traces for g=0 (silence), $g=54\,\mathrm{nS}$ (bursting), $g=85\,\mathrm{nS}$ (chaotic), and $g=114\,\mathrm{nS}$ (tonic).

constructed the bifurcation diagram shown in Fig. 8. This diagram displays remarkable similarities with the corresponding computational bifurcation diagram of Fig. 5. In Fig. 8, no spikes are present for small values of the conductance up to $g_{MI} = 38$ nS, at which point a double band of interspike intervals emerges as was the case in Fig. 5. Further increase in g_{MI} values results in a decrease in interspike intervals. At $g_{MI} = 78$ nS, the two bifurcation bands merge into one wide single band which then thins down at $g_{MI} = 105 \text{ nS}$ and continues so for increasing g_{MI} . These four distinct regions in the bifurcation diagram (silence, double band, wide single band, thin single band) are the same regions encountered in the model bifurcation diagram of Fig. 5 as well as in the noiseless bifurcation diagram of Fig. 4. The graph in Fig. 8 showing the firing rate of the biological neuron displays the same trends exhibited in the graphs of Fig. 5, as well as in Fig. 4, except that the noiseless diagram firing rate displays the typical kink downward in the chaotic transition between bursting and tonic behaviors. The ISI histogram for the experimental data (Fig. 8 inset) shows two peaks similar to the ISI histograms for larger noise intensities [Figs. 5(b) and 5(c)] instead of showing more peaks referring to other periods. A magnification

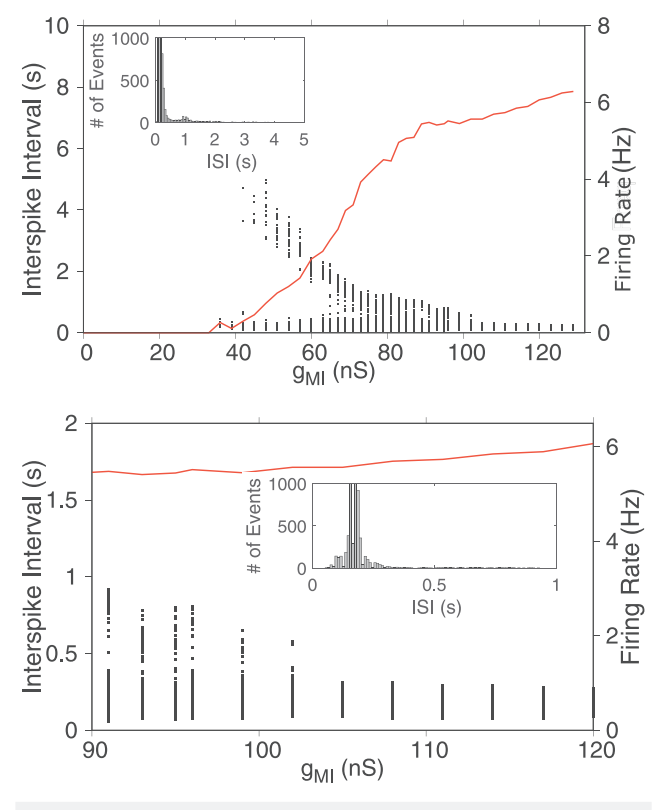


FIG. 8. Top: experimental bifurcation diagram and firing rate for the biological neuron with g_{Ml} as control parameter and corresponding histogram (inset). This graph shows the output of 1 out of 9 experiments, all displaying the same overall features. Bottom: A magnification of the above bifurcation diagram with the corresponding histogram (inset).

of the experimental bifurcation diagram with the corresponding ISI histogram is shown in Fig. 8 bottom graph. There seems to be two very close peaks in the histogram suggesting a period-2 around that range, however we were not able to find such evidence in the experimental traces.

The bursting-tonic transition is observed in all three settings shown in Figs. 4, 5, and 8. However, the chaos/period-doubling feature of the transition is lost in both Figs. 5 and 8, suggesting that noise absorbs the intrinsic chaotic behavior of the neuron. Given the typical erratic characteristics of chaos and noise, albeit each resulting from very distinct mechanisms, it constitutes a difficult task separating them once they are mixed.

VI. POINCARÉ MAPPING

A Poincaré map can be constructed from the trajectory of a dynamical system in its phase space, as it intersects a lower dimensional subspace, with each crossing point being sent to the next. The lower dimensional dynamical system thus obtained is discrete and preserves the major properties of the original higher dimensional system. This technique for constructing return maps is proven to

be useful when analyzing data outputs from complex systems and processes.

Return maps of the noiseless computational, noisy computational, and experimental data in a lower dimensional space are depicted in the graphs of Fig. 9, using their respective interspike intervals. The four return maps for each system are lined up horizontally with increasing values of g_{MI} as indicated. For the noiseless computational model (first row) the maps are clean, yielding typical maps for neuronal bursting for $g_{MI} = 0.34 \,\mathrm{mS/cm^2}$, chaotic for $g_{MI} = 0.3542 \,\text{mS/cm}^2$ (check Fig. 4 in Ref. 46), periodic for $g_{MI} = 0.358 \,\mathrm{mS/cm^2}$, and tonic for $g_{MI} = 0.36 \,\mathrm{mS/cm^2}$. The corresponding noisy computational and experimental Poincaré maps are plotted in the two lower rows in the same figure, in the same order of increasing g_{MI} values, exhibiting the same overall features as the maps on the first row. These results further support the hypothesis that the experimental PD neuron undergoes the same bursting-tonic transition that both the noiseless and the noisy computational neurons go through. The computational noiseless and noisy neurons are more amenable to be scrutinized than the experimental biological neuron, where the chaos mediated bursting-tonic transition is not apparent. However, the noisy and noiseless computational outcomes

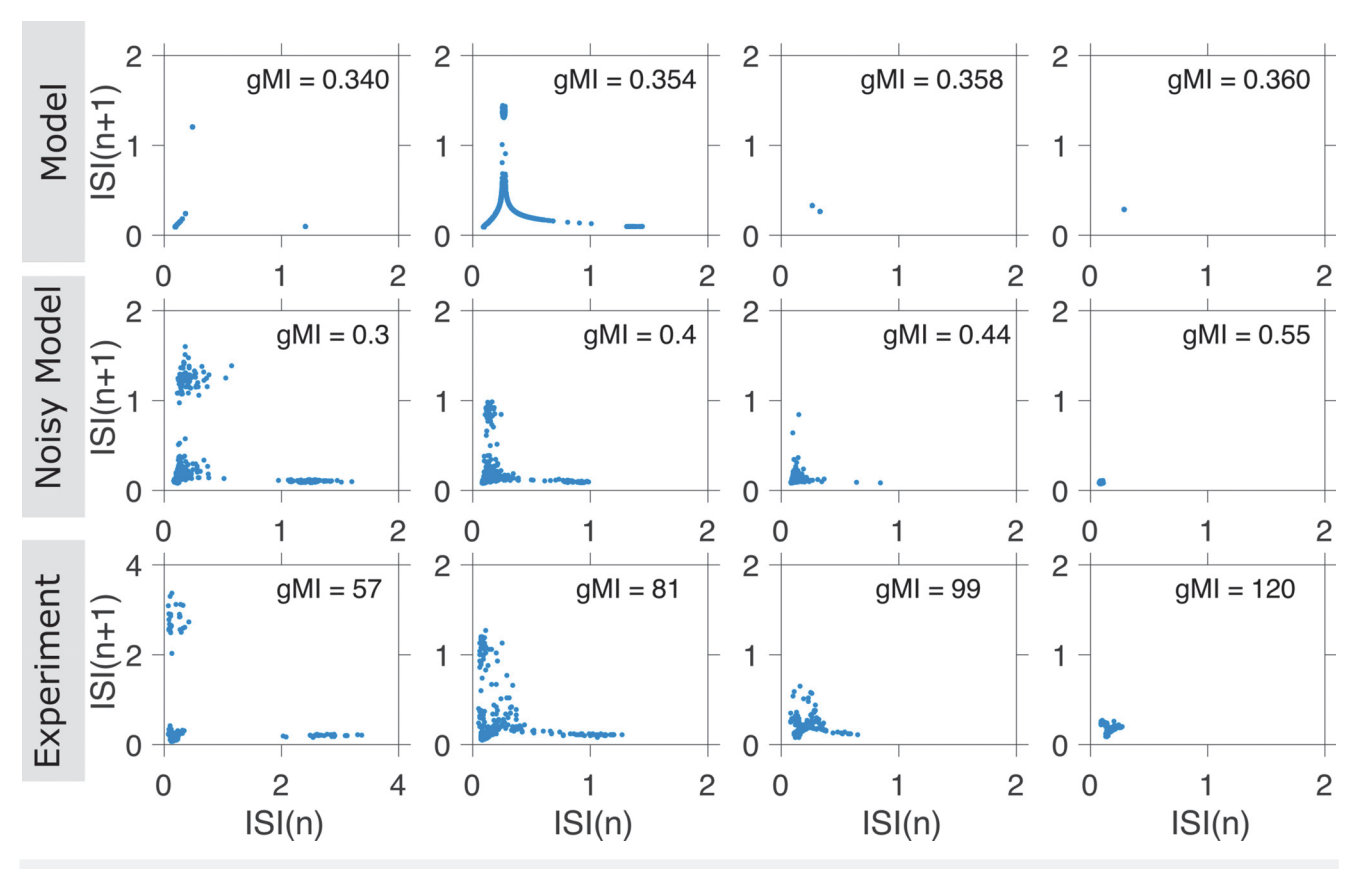


FIG. 9. Return maps of the noiseless model (first row), the noisy model (second row) and the experimental neuron (third row), with their corresponding g_{MI} values as indicated.

strongly suggest that the chaos mediated transition is also likely present in the noisy model, but hidden in the midst of the intrinsic stochasticity of the biological neuron.

VII. CONCLUDING REMARKS

Transitions between different activity states are ubiquitously present in neuronal systems, being of crucial relevance in cognition, sleeping cycles, and motor processes. While the individual neuronal states are well known and understood, that is not the case for the transitions taking place between them. In this work, we study the transitions between regimes of bursting and tonic activity found in the stomatogastric nervous system of crustaceans.

We implemented computer simulations using neuronal model equations with physiologically relevant variables and parameters. The model contains a modulatory current, equivalent to a dynamic voltage clamp, which induces neuronal transitions between states of tonic and bursting, mediated by period-doubling cascades and chaos. This type of transition has been observed in computer simulations of neuronal activity in networked neurons in synchronous processes, 9,12 as well as in connection with temperature effects on neuronal behaviors. 11 Also, period doubling bifurcations and transitions mediated by chaos have been found in biological systems, as for example, displaying inherent difficulties with abrupt changes in the response period in flicker vision, 47 in chaos with noise in epidemic outbreaks models, 48 in chaos and stochasticity in heart arrhythmia, 49 and in nonlinearity and chaos in ecology. 50

We introduced noise into the voltage of our model, taking into account that stochasticity is commonly found in natural and biological systems. The inclusion of the noisy term did not change the overall basic features of the tonic and bursting regimes, still showing a transition between the two regimes. However, the period-doubling cascade and chaos transition seen in the noise free model was lost. While the smearing of bifurcations by noise is a known effect,²⁷ our computer simulations provide unique insights about the underlying dynamics hidden in the real neuronal experiments. Nevertheless, extricating chaos from noise has proven to be a very difficult task.^{51–53}

Next, we implemented an *in vitro* experimental dynamic clamp on the pyloric dilator neuron of the crab stomatogastric neuronal system, as a means for inducing bursting-tonic transitions. The results showed striking similarities with the output of our noisy computational model, suggesting that the tonic-bursting transition in the biological neuron might be mediated by chaos, however hidden by noise. While new techniques have been developed to distinguish a chaotic from a noisy signal in computational models, separating one from the other when they are intrinsically mixed remains a challenge, particularly in experimental settings. Chaos may indeed be absorbed by noise.

ACKNOWLEDGMENTS

This work was supported by the National Science Foundation (NSF IOS 1755098) to Wolfgang Stein, the R.D. Weigel Research Grant, the Mockford-Thompson Summer Fellowship, and the ISU Graduate School Merit Fellowship to Josselyn Gonzalez, and the

College of Arts and Sciences Interdisciplinary Award to Epaminondas Rosa and Wolfgang Stein.

AUTHOR DECLARATIONS

Conflict of Interest

The authors have no conflicts to disclose.

Ethics Approval

Ethics approval for experiments reported in the submitted manuscript on animal or human subjects was granted. There is no requirement for experimental ethics approval for the crab *C. borealis* which was the animal used in the experiments.

Author Contributions

Josselyn Gonzalez: Formal analysis (equal); Writing – original draft (equal); Writing – review & editing (equal). Rosangela Follmann: Formal analysis (equal); Writing – original draft (equal); Writing – review & editing (equal). Epaminondas Rosa Jr.: Conceptualization (equal); Formal analysis (equal); Funding acquisition (equal); Writing – original draft (equal); Writing – review & editing (equal). Wolfgang Stein: Conceptualization (equal); Funding acquisition (equal); Writing – original draft (equal); Writing – review & editing (equal).

DATA AVAILABILITY

The data that support the findings of this study are available from the corresponding author upon reasonable request.

APPENDIX: MODEL PARAMETERS

Model parameters are set as follows if not otherwise stated in the text.

```
\begin{split} &V_{0Na} = -25.0 \text{ mV}, \ V_{0K} = -25.0 \text{ mV}, \ V_{0SD} = -40.0 \text{ mV}, \\ &V_{leak} = -60.0 \text{ mV}, \ V_{Na} = 50.0 \text{ mV}, \ V_{K} = -90.0 \text{ mV}, \\ &V_{SR} = -90.0 \text{ mV}, \ V_{SD} = 50.0 \text{ mV}, \\ &g_{leak} = 0.1 \text{ mS/cm}^2, \ g_{Na} = 1.5 \text{ mS/cm}^2, \\ &g_{K} = 2.0 \text{ mS/cm}^2, \ g_{SR} = 0.6 \text{ mS/cm}^2, \\ &g_{SD} = 0.2 \text{ mS/cm}^2, \\ &\tau_{K} = 2.0 \text{ ms}, \ \tau_{SD} = 10.0 \text{ ms}, \ \tau_{SR} = 20.0 \text{ ms}, \\ &s_{Na} = 0.25 \text{ mV}^{-1}, \ s_{K} = 0.25 \text{ mV}^{-1}, \ s_{SD} = 0.09 \text{ mV}^{-1}, \\ &\nu_{acc} = 0.012, \ \nu_{dep} = 0.08, \ \rho = 0.607, \ \phi = 0.124, \\ &I_{ini} = 0.05 \text{ A}. \end{split}
```

REFERENCES

- ¹H. Poincaré, *Oeuvres de Henri Poincaré* (Gauthier-Villars et cie, 1916), Vol. 1.
 ²E. N. Lorenz and K. Haman, "The essence of chaos," Pure Appl. Geophys. 147, 598–599 (1996).
- ³L. Glass and M. C. Mackey, "From clocks to chaos," in *From Clocks to Chaos* (Princeton University Press, 2020).
- ⁴I. Prigogine and I. Stengers, *Order Out of Chaos: Man's New Dialogue with Nature* (Verso Books, 2018).
- ⁵E. Ott, Chaos in Dynamical Systems (Cambridge University Press, 2002).
- ⁶S. H. Strogatz, Nonlinear Dynamics and Chaos: With Applications to Physics, Biology, Chemistry, and Engineering (CRC Press, 2018).

- ⁷L. Lovejoy, P. Shepard, and C. Canavier, "Apamin-induced irregular firing *in vitro* and irregular single-spike firing observed *in vivo* in dopamine neurons is chaotic," Neuroscience **104**, 829–840 (2001).
- ⁸E. M. Izhikevich, Dynamical Systems in Neuroscience (MIT Press, 2007).
- ⁹E. Rosa, Q. M. Skilling, and W. Stein, "Effects of reciprocal inhibitory coupling in model neurons," Biosystems 127, 73–83 (2015).
- ¹⁰ A. Shaffer, A. L. Harris, R. Follmann, and E. Rosa, Jr., "Bifurcation transitions in gap-junction-coupled neurons," Phys. Rev. E 94, 042301 (2016).
- ¹¹ M. Burek, R. Follmann, and E. Rosa, "Temperature effects on neuronal firing rates and tonic-to-bursting transitions," Biosystems **180**, 1–6 (2019).
- ¹²R. Follmann, A. Shaffer, Z. Mobille, G. Rutherford, and E. Rosa, "Synchronous tonic-to-bursting transitions in a neuronal hub motif," Chaos: An Interdisciplinary Journal of Nonlinear Science 28, 106315 (2018).
- ¹³S. Sherman, "Tonic and burst firing: Dual modes of thalamocortical relay," Trends Neurosci. **24**, 122–126 (2001).
- ¹⁴R. R. Llinás and M. Steriade, "Bursting of thalamic neurons and states of vigilance," J. Neurophysiol. 95, 3297–3308 (2006).
- ¹⁵A. Frigon, "Central pattern generators of the mammalian spinal cord," Neuroscientist 18, 56–69 (2012).
- ¹⁶S. Grillner, "Control of locomotion in bipeds, tetrapods, and fish," Compr. Physiol. 1, 1179–1236 (2011).
- ¹⁷P. Rosenbaum, J. Schmitz, J. Schmidt, and A. Büschges, "Task-dependent modification of leg motor neuron synaptic input underlying changes in walking direction and walking speed," J. Neurophys. 114, 1090–1101 (2015).
- ¹⁸M. P. Nusbaum, D. M. Blitz, and E. Marder, "Functional consequences of neuropeptide and small-molecule co-transmission," Nat. Rev. Neurosci. 18, 389–403 (2017)
- 19W. Stein, "Stomatogastric nervous system," in Oxford Research Encyclopedia of Neuroscience (Oxford Research Encyclopedias, 2017).
- ²⁰N. Daur, F. Nadim, and D. Bucher, "The complexity of small circuits: The stomatogastric nervous system," Curr. Opin. Neurobiol. 41, 1–7 (2016).
- ²¹ M. P. Nusbaum and D. M. Blitz, "Neuropeptide modulation of microcircuits," Curr. Opin. Neurobiol. **22**, 592–601 (2012).
- ²²E. Marder and V. Thirumalai, "Cellular, synaptic and network effects of neuro-modulation," Neural Netw. 15, 479–493 (2002).
- ²³ M. I. Rabinovich, H. D. Abarbanel, R. Huerta, R. Elson, and A. I. Selver-ston, "Self-regularization of chaos in neural systems: Experimental and theoretical results," IEEE Trans. Circuits Syst. I: Fundam. Theory Appl. 44, 997–1005 (1997).
- ²⁴D. Takeshita, Y. D. Sato, and S. Bahar, "Transitions between multistable states as a model of epileptic seizure dynamics," Phys. Rev. E 75, 051925 (2007).
- ²⁵W. Braun, B. Eckhardt, H. A. Braun, and M. Huber, "Phase-space structure of a thermoreceptor," Phys. Rev. E **62**, 6352 (2000).
- ²⁶F. Buchholtz, J. Golowasch, I. R. Epstein, and E. Marder, "Mathematical model of an identified stomatogastric ganglion neuron," J. Neurophysiol. **67**, 332–340 (1992)
- ²⁷H. Braun, M. Huber, M. Dewald, K. Schäfer, and K. Voigt, "Computer simulations of neuronal signal transduction: The role of nonlinear dynamics and noise," Int. J. Bifurcat. Chaos **8**, 881–889 (1998).
- ²⁸C. Finke, J. A. Freund, E. Rosa, Jr., P. H. Bryant, H. A. Braun, and U. Feudel, "Temperature-dependent stochastic dynamics of the Huber–Braun neuron model," Chaos **21**, 047510 (2011).
- ²⁹S. Postnova, E. Rosa, and H. Braun, "Neurones and synapses for systemic models of psychiatric disorders," Pharmacopsychiatry 43, S82–S91 (2010).
- ³⁰V. Thirumalai and E. Marder, "Colocalized neuropeptides activate a central pattern generator by acting on different circuit targets," J. Neurosci. **22**, 1874–1882 (2002).

- ³¹ W. Stein, "Modulation of stomatogastric rhythms," J. Comp. Physiol. A 195, 989–1009 (2009).
- ³²M. P. Nusbaum and E. Marder, "A modulatory proctolin-containing neuron (MPN). II. State-dependent modulation of rhythmic motor activity," J. Neurosci. 9, 1600–1607 (1989).
- ³³J. Golowasch and E. Marder, "Proctolin activates an inward current whose voltage dependence is modified by extracellular Ca²⁺," J. Neurosci. **12**, 810–817 (1992)
- ³⁴C. Städele, S. Heigele, and W. Stein, "Neuromodulation to the rescue: Compensation of temperature-induced breakdown of rhythmic motor patterns via extrinsic neuromodulatory input," PLoS Biol. 13, e1002265 (2015).
- ³⁵B. Drukarch, H. A. Holland, M. Velichkov, J. J. Geurts, P. Voorn, G. Glas, and H. W. de Regt, "Thinking about the nerve impulse: A critical analysis of the electricity-centered conception of nerve excitability," Prog. Neurobiol. 169, 172–185 (2018).
- ³⁶R. L. Calabrese, "Neuronal networks: Degeneracy unleashed," Curr. Biol. 31, R1439–R1441 (2021).
- ³⁷ A. M. Swensen and E. Marder, "Multiple peptides converge to activate the same voltage-dependent current in a central pattern-generating circuit," J. Neurosci. **20**, 6752–6759 (2000).
- ³⁸S. Postnova, B. Wollweber, K. Voigt, and H. Braun, "Impulse pattern in bidirectionally coupled model neurons of different dynamics," Biosystems 89, 135–142 (2007).
- ³⁹U. Feudel, A. Neiman, X. Pei, W. Wojtenek, H. Braun, M. Huber, and F. Moss, "Homoclinic bifurcation in a Hodgkin–Huxley model of thermally sensitive neurons," Chaos 10, 231–239 (2000).
- ⁴⁰ J. P. Keener and J. Sneyd, *Mathematical Physiology* (Springer, 1998), Vol. 1.
- ⁴¹A. A. Faisal, L. P. Selen, and D. M. Wolpert, "Noise in the nervous system," Nat. Rev. Neurosci. **9**, 292–303 (2008).
- A. Shaffer, R. Follmann, A. L. Harris, S. Postnova, H. Braun, and E. Rosa, "A critical firing rate associated with tonic-to-bursting transitions in synchronized gap-junction coupled neurons," Eur. Phys. J. Spec. Top. 226, 1939–1951 (2017).
 S. L. Hooper and E. Marder, "Modulation of a central pattern generator by two
- ⁴³S. L. Hooper and E. Marder, "Modulation of a central pattern generator by two neuropeptides, proctolin and fmrfamide," Brain Res. 305, 186–191 (1984).
- ⁴⁴ A. A. Prinz, L. Abbott, and E. Marder, "The dynamic clamp comes of age," Trends Neurosci. 27, 218–224 (2004).
- ⁴⁵A. A. Sharp, M. B. O'Neil, L. Abbott, and E. Marder, "The dynamic clamp: Artificial conductances in biological neurons," Trends Neurosci. 16, 389–394 (1993)
- ⁴⁶E. N. Lorenz, "Deterministic nonperiodic flow," J. Atmos. Sci. **20**, 130–141 (1963)
- ⁴⁷D. W. Crevier and M. Meister, "Synchronous period-doubling in flicker vision of salamander and man," J. Neurophysiol. 79, 1869–1878 (1998).
- ⁴⁸L. Billings and I. Schwartz, "Exciting chaos with noise: Unexpected dynamics in epidemic outbreaks," J. Math. Biol. 44, 31–48 (2002).
- ⁴⁹Z. Qu, G. Hu, A. Garfinkel, and J. N. Weiss, "Nonlinear and stochastic dynamics in the heart," Phys. Rep. **543**, 61–162 (2014).
- ⁵⁰O. N. Bjørnstad, "Nonlinearity and chaos in ecological dynamics revisited," Proc. Natl. Acad. Sci. U.S.A. 112, 6252–6253 (2015).
- ⁵¹O. A. Rosso, H. A. Larrondo, M. T. Martin, A. Plastino, and M. A. Fuentes, "Distinguishing noise from chaos," Phys. Rev. Lett. 99, 154102 (2007).
- 52T. Tél, Y.-C. Lai, and M. Gruiz, "Noise-induced chaos: A consequence of long deterministic transients," Int. J. Bifurcat. Chaos 18, 509–520 (2008).
- ⁵³T. He and S. Habib, "Chaos and noise," Chaos **23**, 033123 (2013).
- ⁵⁴Q. Li, Z. Fu, and N. Yuan, "Beyond Benford's law: Distinguishing noise from chaos," PLoS One 10, e0129161 (2015).